



Structure analysis of vitusite glass–ceramic waste forms using extended X-ray absorption fine structures



Mi Ae Kim^a, Jay Hyok Song^b, Wooyong Um^{c,d}, Neil Hyatt^e, Shi-Kuan Sun^e, Jong Heo^{a,c,*}

^a Department of Materials Science and Engineering, Pohang University of Science and Technology (POSTECH), Pohang, Gyeongbuk 790-784, South Korea

^b Energy1 Lab., Corporate R & D center, Samsung SDI, Yongin, South Korea

^c Division of Advanced Nuclear Engineering, Pohang University of Science and Technology (POSTECH), Pohang, Gyeongbuk 790-784, South Korea

^d Pacific Northwest National Laboratory, Richland, WA 99354, United States

^e Department of Materials Science and Engineering, University of Sheffield, Sir Robert Hadfield Building, Mappin Street, Sheffield S1 3JD, United Kingdom

ARTICLE INFO

Keywords:

Extended X-ray absorption fine structure spectroscopy
Waste forms
Vitusite glass-ceramics
Vitrification
Pyro-processing

ABSTRACT

Vitusite glass–ceramic waste forms were developed and the local environments of the Nd³⁺ ions in the waste forms were analyzed using extended X-ray absorption fine structure (EXAFS) spectroscopy. A second shell was observed in the Fourier transform (FT) of the EXAFS Nd L_{III}-edge spectra with the formation of vitusite crystals in the glass matrix. This second shell was attributed to the presence of the Nd–P and Nd–Na ion pairs constituting the vitusite crystal. The preferred incorporation of Nd³⁺, P⁵⁺, and Na⁺ inside the crystalline phases surrounded by the glass matrix increased the chemical durability of the glass–ceramics.

1. Introduction

Pyro-processing technology is used to recover radioactive uranium and trans-uranium elements from the spent fuels of pressurized water reactors [1–3]. Several hazardous wastes are also produced during pyro-processing that should be transformed into stable materials for safe storage. The compositions of these wastes obtained after pyro-processing significantly differ from those generated from commercial nuclear power plants [4,5]. In particular, wastes resulting from the electro-winning stage of the pyro-processing process consist of eight rare earth (RE) oxides, primarily CeO₂ and Nd₂O₃, which are unlike any other waste obtained from nuclear reactors [4]. Therefore, specific waste forms need to be developed to immobilize wastes containing high concentrations of these rare-earth oxides.

Glass–ceramics (GCs) are polycrystalline materials produced through carefully designed heat treatment techniques to control the crystallization of the base glasses [6,7]. GCs consist of an amorphous phase together with one or more pre-designed crystalline phases. GCs are easier to fabricate than ceramics because of the requirement of fewer processes such as pressing and sintering. Concentrations of RE ions inside the crystalline phases are known to be much higher than those in the glass matrix [6]. Therefore, GCs can be used as potential hosts for immobilizing RE ions in the pyro-processing wastes. Among several potential crystalline phases, the vitusite [Na₃RE(PO₄)₂] crystal

offers promising characteristics because it can accommodate a large number of RE ions [8]. In addition, these GCs exhibit low volatilization of major constituents, high waste loading, and high chemical durability [8]. In fact, the chemical composition of the vitusite crystal suggests that approximately 80 wt% of its crystalline phases can comprise RE ions. Despite the significant potential of vitusite in terms of storing pyro-processing wastes, the local structure of RE ions in vitusite GCs has not yet been clearly understood. In this study, we prepared vitusite GCs and investigated the effects of the heat treatment temperature on the local structure of RE ions in the vitusite GCs to understand the mechanism of RE dissolution inside the crystals.

2. Materials and methods

2.1. Materials preparation

In our previous study, CeO₂ and Nd₂O₃ were used as representatives of the eight RE oxide wastes generated in pyro-processing, because these two components constitute 62 mol% of the total wastes [8]. However, extended X-ray absorption fine structure (EXAFS) spectra from the Ce L_{III} edge (5730 eV) and the Nd L_{III} edge (6208 eV) are difficult to distinguish as these are observed at similar energy ranges. Therefore, CeO₂ was replaced by Nd₂O₃ in the present study to simplify the analysis. A glass having a nominal composition

* Correspondence to: Department of Materials Science and Engineering and Division of Advanced Nuclear Engineering, Pohang University of Science and Technology, Pohang, Gyeongbuk 790-784, Republic of Korea.

E-mail address: jheo@postech.ac.kr (J. Heo).

<http://dx.doi.org/10.1016/j.ceramint.2016.12.129>

Received 6 November 2016; Received in revised form 26 December 2016; Accepted 28 December 2016

Available online 29 December 2016

0272-8842/ © 2017 The Authors. Published by Elsevier Ltd.

This is an open access article under the CC BY license (<http://creativecommons.org/licenses/by/4.0/>).

(mol%) of $46.5\text{SiO}_2\text{--}28.4\text{Na}_2\text{O--}11.5\text{B}_2\text{O}_3\text{--}8.0\text{Li}_2\text{O--}3.6\text{Nd}_2\text{O}_3\text{--}5.4\text{P}_2\text{O}_5$ was prepared. The ratio of RE to P was fixed to be 1:1.5 based on the glass-forming ability and possible phase separation in glasses containing large amount of P_2O_5 [8,9]. The precursors were weighed and mixed in a miller for 5 h before melting in an alumina crucible at $1300\text{ }^\circ\text{C}$ for 30 min. The melt was quenched by pouring it onto a brass mold, in air. The as-prepared bulk-glass samples were then heat-treated at $600\text{ }^\circ\text{C}$ or $800\text{ }^\circ\text{C}$ for 3 h to precipitate vitusite crystals based on the preliminary experiments.

2.2. X-ray diffraction (XRD) analyses

The GCs were ground to fine powders using a mortar and pestle. The powders were then used for recording XRD (RIGAKU, D/MAX-2500) patterns. The X-ray source was $\text{Cu K}\alpha$ ($\lambda=0.1541\text{ nm}$) with the voltage and current of the generator as 40 kV and 100 mA , respectively. Diffraction patterns were compared to those of the Joint Committee of Powder Diffraction Standards database. For performing quantitative phase analysis, we added 10 wt% of an internal standard (MgO) to the specimen heat-treated at $800\text{ }^\circ\text{C}$. Diffraction patterns were recorded in the 2θ range of $10\text{--}110^\circ$ with a step size of 0.02 and a duration time of 2 s . The GSAS software [10] was used to refine the XRD patterns and calculate the phase fractions of the vitusite and amorphous phases.

2.3. EXAFS analysis

EXAFS measurements were conducted at the HF-XAFS (10C) beam line at Pohang Light Source (PLS) at POSTECH, Korea. Two (111) silicon crystal monochromators were positioned such that the incident beam intensity would be maximized. They were further optimized to reduce the spectra corresponding to the overtone of the crystals of the monochromator that appear near the Nd L_{III} edge energy (6208 eV). A slit size of $1.0\times 4.0\text{ mm}$ was used, and the detectors for the incident and transmitted beams were filled with 100% He and 25 vol% $\text{N}_2/75\text{ vol}\%$ He, respectively. The amount of the powdered specimens spread on adhesive tape was carefully adjusted to obtain a clear jump at the near-edge energies. The EXAFS spectra from the specimens of the glass and GCs were recorded in transmission mode. The absorption coefficient, μ , near the Nd L_{III} edge was calculated using Lambert's law [Eq. (1)] [11].

$$I_t/I_0 = \exp(-\mu x) \quad (1)$$

where I_0 and I_t are the intensities of the incident and transmitted beams, respectively and x corresponds to the thickness of the specimens. The background of the spectrum was subtracted by a polynomial fitting of pre- and post-edge regions using the Athena program in the IFFEFFIT software package [12], and the spectra were further normalized in the energy range of $150\text{--}450\text{ eV}$. The background parameter (Rbkg) was set as 0.13 nm to remove the virtual spectra appearing within 0.13 nm from the core atom following the general procedures for the analysis of the EXAFS spectra [13–15]. Fourier transform (FT) was performed using a Hanning window in a k -range of approximately $24\text{--}85\text{ nm}^{-1}$. ATOMS and FEFF programs in Artemis were employed for obtaining structural information such as the effective scattering amplitudes, phase shifts, mean free paths, and the initial path lengths. The global amplitude reduction factor was determined to be unity. All the variables, such as the interatomic distance, the Debye–Waller factor, and coordination number (CN), were kept floating during the fitting procedures for the first peak (R range of $0.13\text{--}0.30\text{ nm}$). For the fitting that included both the first and second shells (R range of $0.13\text{--}0.40\text{ nm}$), it was necessary to consider three different atomic pairs (Nd–O, Nd–P, and Nd–Na). CNs were set first based on the information obtained from the Vesta; the interatomic distances and the Debye–Waller factors remained as variables. The R-factor that quantified the goodness-of-fit was less than 0.03 for all fits.

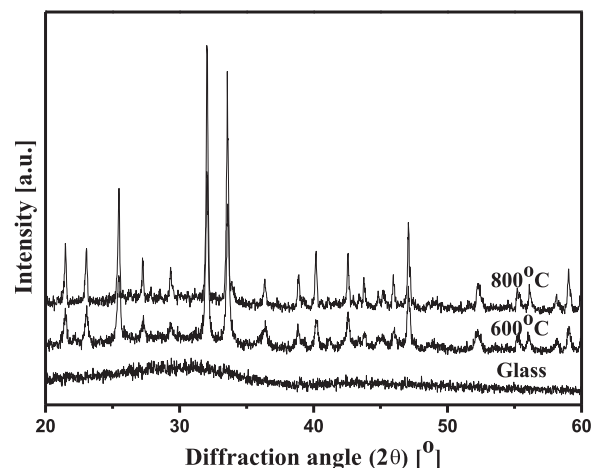


Fig. 1. XRD patterns of the as-prepared glass and GCs after heat treating at $600\text{ }^\circ\text{C}$ and $800\text{ }^\circ\text{C}$ for 3 h and diffraction lines from $\text{Na}_3\text{Nd}(\text{PO}_4)_2$ (PDF# 38-0058).

3. Results and discussion

3.1. Formation of vitusite GCs

The XRD patterns of the heat-treated specimens (Fig. 1) showed clear peaks corresponding to vitusite crystals only [8]. Thus, vitusite GCs were formed even after replacing CeO_2 with Nd_2O_3 . Phase-fraction analysis using the GSAS software on the specimen containing 10 wt% of the internal standard (MgO) indicated that the phase fractions of the vitusite and MgO crystals were $70.0 (\pm 0.08)$ and $30.0 (\pm 0.2)$ wt%, respectively ($R_{\text{wp}}=0.0633$ and $R_p=0.0442$). The mass fractions of the vitusite crystals and the amorphous phase (excluding the standard) were estimated to be 25.9 and $74.1\text{ wt}\%$, respectively, using the following equations:

$$c = c_{\text{gsas}} \left(\frac{s}{s_{\text{gsas}}} \right) \left(\frac{100}{100-s} \right) \quad (2)$$

$$a = (100 - c) \quad (3)$$

where c (wt%) and a (wt%) correspond to the crystal and amorphous phase fractions, respectively, in the specimen, and c_{gsas} (wt%) and s_{gsas} (wt%) correspond to the phase fractions of the crystals and the standard material obtained using the GSAS software.

3.2. Analyses of the XANES and EXAFS spectra

The Nd L_{III} -edge XANES spectra of the Nd_2O_3 powders, the as-prepared glass, and the GCs heat-treated at $600\text{ }^\circ\text{C}$ and $800\text{ }^\circ\text{C}$ are shown in Fig. 2. All four spectra have similar features, suggesting that the Nd chemistry in our specimens is similar to that in the Nd_2O_3 powder. In addition, the edge positions are same in all specimens, indicating that Nd exists in the form of Nd^{3+} in the all specimens as it does in Nd_2O_3 .

The FT L_{III} -edge EXAFS spectra of Nd^{3+} ions in the glass and GC samples heat-treated at $600\text{ }^\circ\text{C}$ and $800\text{ }^\circ\text{C}$ are shown in Fig. 3. The peak positions on the reduced distance scale used in Figs. 3–5 are smaller than the true interatomic distances due to a phase contribution in the EXAFS equation. We used a constant value of 0.04 nm following the general convention [16], even though the value changed slightly for different pairs. A shell centered at a reduced distance of $\sim 0.24\text{ nm}$ is clearly observed for all the specimens. An additional shell is observed only for the GCs at $\sim 0.36\text{ nm}$ in the phase-corrected FT. The FT results were obtained by substituting all possible first- and second-neighbor pairs with Nd. The best fit from among those was selected by considering the R-factor (a measure of the agreement between the model and the experimental data [17]) and the physical meanings of

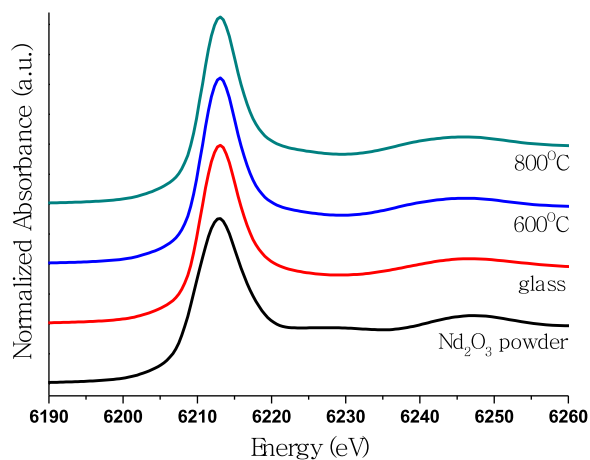


Fig. 2. Nd L_{III} -edge XANES of Nd_2O_3 powder and as-prepared glass and GCs heat-treated at 600 °C and 800 °C.

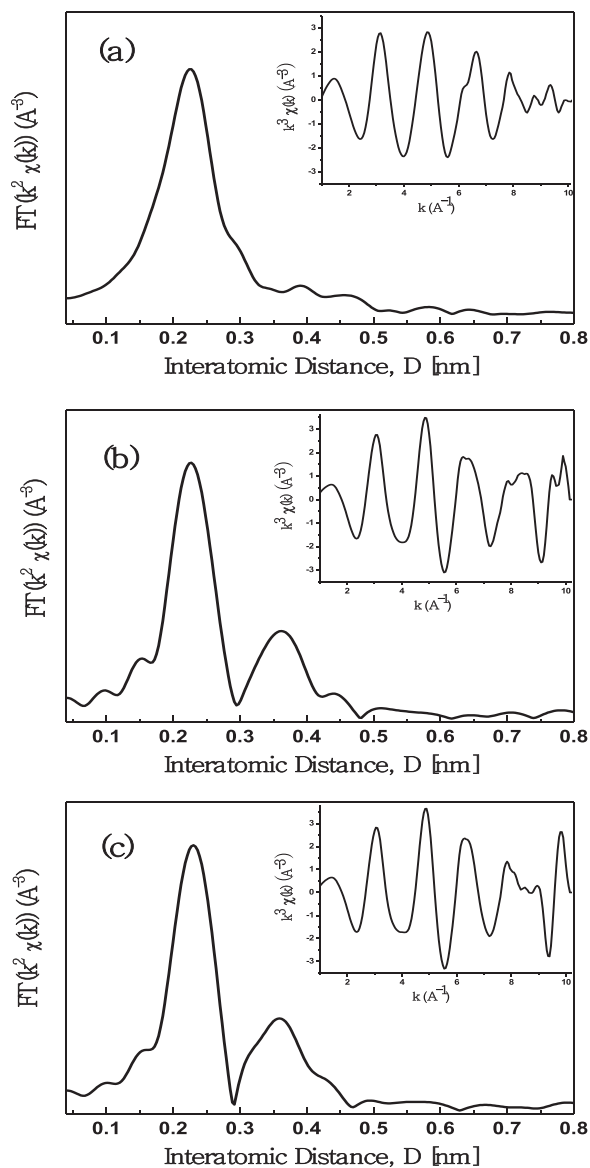


Fig. 3. Fourier transform of Nd L_{III} -edge EXAFS spectrum of (a) as-prepared glass and GCs heat-treated at (b) 600 °C and (c) 800 °C. Inset: The EXAFS spectra in k -space of the same specimens.

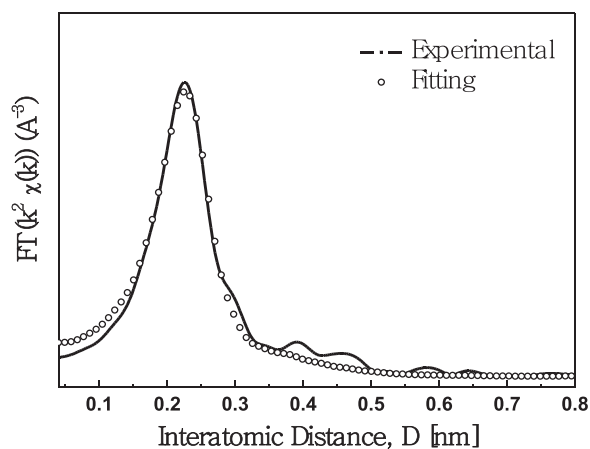


Fig. 4. Fourier transform of Nd L_{III} -edge EXAFS spectrum (solid line) obtained with the as-prepared glass and the results of fitting (circle) for the first shell around Nd ions.

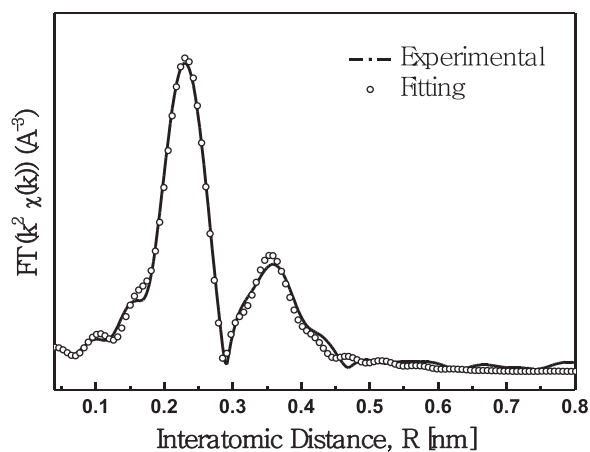


Fig. 5. Fourier transform of Nd L_{III} -edge EXAFS spectrum (solid line) of GCs heat-treated at 800 °C and the corresponding fitted curve (circle) using Nd–Na and Nd–P paths for the second shells surrounding Nd ions.

Table 1

Interatomic distances (D) [nm], coordination numbers (CN), and Debye–Waller factors (σ^2) of the first shell fitted from the glass and GC specimens.

Specimens	D (nm)	CN	Σ^2 (nm)
As prepared glass	0.24 (± 0.02)	6.7 (± 0.51)	$1.8 \cdot 10^{-4}$ ($\pm 5 \cdot 10^{-5}$)
Glass ceramics			
HT 600 °C	0.24 (± 0.02)	6.9 (± 1.41)	$1.8 \cdot 10^{-4}$ ($\pm 5 \cdot 10^{-5}$)
HT 800 °C	0.25 (± 0.02)	6.9 (± 1.31)	$1.8 \cdot 10^{-4}$ ($\pm 5 \cdot 10^{-5}$)

the results. The fitting results indicate that the first shell is associated with the Nd–O pair in the glass (R -factor=0.0056) and GCs (Figs. 4 and 5). The distances between atoms (D), the CNs of the O atoms surrounding Nd^{3+} , and the Debye–Waller factors (σ^2) of the first shell are 0.24–0.25 nm, 6.7–6.9, and $\sim 8 \cdot 10^{-4}$ nm², respectively (Table 1). As the heat-treatment temperature increased from 600 °C to 800 °C, the changes in the distance between Nd and O atoms and the CNs were all within the experimental error.

Analysis of the second shell was more difficult owing to the weak signal intensities and complexities of the possible bonding schemes. The potential second-nearest neighbors of the vitusite crystal [$Na_3RE(PO_4)_2$] are Nd–Nd, Nd–Na, and Nd–P. However, the Nd–Nd distances either reported earlier (> 0.4 nm) [17–20] or obtained using the Vesta software (~ 0.48 nm) are significantly longer than the corresponding distance from the second shell (~ 0.35 nm) observed in

Table 2

Results obtained with the fitting of first and second shells for the specimen heat-treated at 800 °C.

Atom pairs	<i>D</i> (nm)	CN	σ^2 (nm ²)
Nd–O pair	0.25 (\pm 0.02)	7.1 ^a	$1.4 \cdot 10^{-4}$ (\pm $1 \cdot 10^{-5}$)
Nd–P pair	0.32 (\pm 0.03)	4.4 ^a	$2.7 \cdot 10^{-4}$ (\pm $9 \cdot 10^{-5}$)
Nd–Na pair	0.36 (\pm 0.03)	6.6 ^a	$2.6 \cdot 10^{-4}$ (\pm $1 \cdot 10^{-4}$)

^a Values obtained with the Vesta software [21].

Fig. 5. The fitting results (R-factor=0.0244) obtained by considering the combination of Nd–P and Nd–Na pairs appear to be the most reasonable (Fig. 5). The distances of the interatomic Nd–P and Nd–Na pairs obtained by fitting were 0.32 nm and 0.36 nm, respectively. The values of CN and σ^2 were calculated from the fitting in the R-space of the EXAFS spectra recorded from the GCs heat-treated at 800 °C (Table 2). The CNs of each pair were determined from the values obtained from the Vesta software [21] to reduce the fitting variables. This result clearly indicates that the Nd–O polyhedrons were surrounded by Na and P ions after the vitusite crystals were formed.

3.3. Proposed structural model of vitusite in GCs

The average Nd–O distance in neodymium oxide (Nd₂O₃) is 0.238 nm, with six CNs of oxygen surrounding Nd³⁺ [22]. Nd³⁺ ions in borosilicate glass are known to be surrounded by approximately eight non-bridging oxygen atoms with a Nd–O distance (*D*) of 0.246 (\pm 0.003) nm, and no Nd–Nd bonds shorter than 0.4 nm are present [18]. On the other hand, in phosphate glass, the Nd–O distance is 0.240–0.237 nm, with the CNs varying in the range of 6.4–9 [19]. These values depend on the Nd₂O₃/P₂O₅ ratios because isolated Nd polyhedra are transformed to clustered Nd polyhedra by sharing oxygen atoms as the Nd₂O₃/P₂O₅ ratio increases. Analysis of the vitusite crystal structure indicates that isolated NdO_{*y*} polyhedra (6 ≤ *y* ≤ 8) are connected to phosphate tetrahedra, with Na⁺ ions acting as charge compensators [20]. In this crystal, the CNs of oxygen atoms

Table 3

Parameters obtained for the vitusite crystal calculated with the Vesta program.

	Nd–O	Nd–P	Nd–Na
Average interatomic distance (nm)	0.25	0.34	0.37
Effective coordination number	7.1	4.4	6.6

surrounding Nd³⁺ are 6–8, and the interatomic distances of Nd–O and Nd–Nd pairs are 0.269 nm and 0.465 nm, respectively. A Nd–O interatomic distance of ~0.24 nm and a CN of ~7 were obtained from the first shell fitting, which matched well with the structure of the vitusite crystal.

Using the atomic displacement data (.cif file) obtained from the crystal structure database of American Mineralogist [23], the vitusite crystal structure was constructed using the Vesta software [21], and the results are shown in Fig. 6. Unit cell parameters of *a*=0.533560 nm, *b*=1.867220 nm, and *c*=1.405460 nm with the space group *Pca*21 were used. Edge-sharing Nd₂O₁₄ dimers (i.e., NdO₈–NdO₈) are interconnected by PO₄ units with a Nd–Nd distance of 0.48 nm. An average of 6.6 Na⁺ ions are located approximately 0.35–0.37 nm from the Nd atoms. The distances of Nd–P pairs are approximately 0.32–0.35 nm with a CN of 4.4 (Table 3).

The Nd–O distances shown in Fig. 6 are not uniform in nature. Among the eight O²⁻ ions surrounding Nd³⁺, six O²⁻ ions are located 0.25 nm from Nd³⁺, which is in agreement with the value obtained from the EXAFS fit. The other two oxygen ions are found at a distance of ~0.28 nm, which corresponds to an edge that is shared with two NdO₈. Because of the presence of two different Nd–O distances, the CNs of oxygen in the first shell calculated from the EXAFS spectra are 6.7–6.9 rather than 8.0. Nevertheless, the EXAFS analysis of the vitusite GC waste forms reasonably reveals the actual structure of the vitusite crystal.

Sodium ions are essential for the formation of the vitusite crystal as they act as charge compensators of Nd₂O₁₄ dimers. In general, Na⁺ ions are evenly distributed throughout the glass to compensate for the

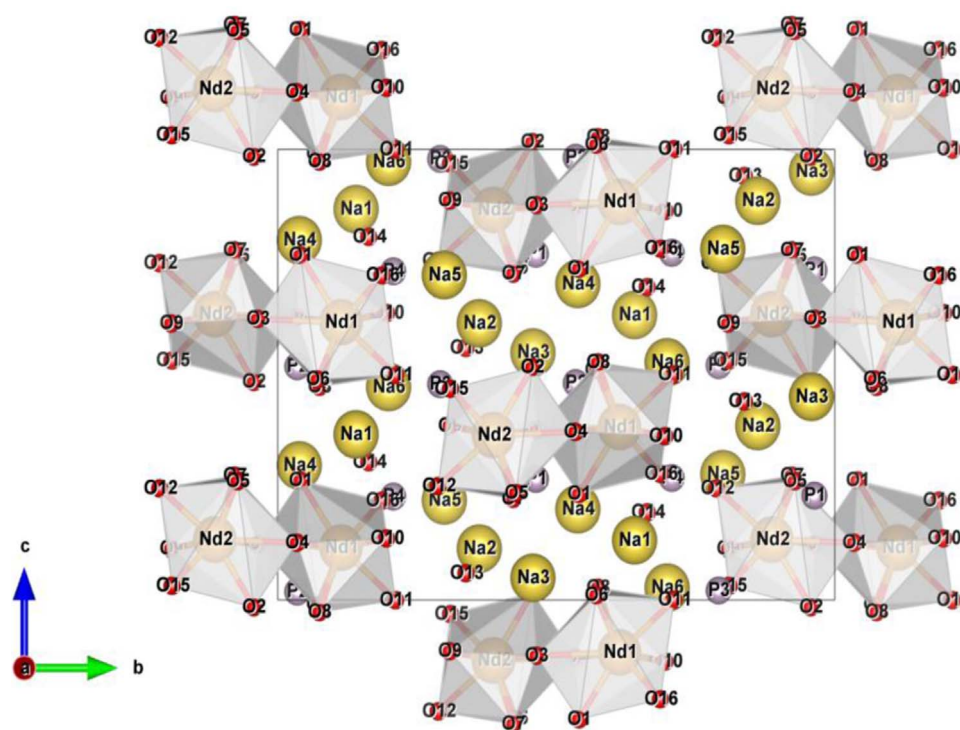


Fig. 6. Representative illustration of the vitusite crystal structure viewed normal to the *b*–*c* plane. The NdO₈ irregular dodecahedra (gray), P atoms (light purple), and Na atoms (yellow) are shown.

negative charges of the non-bridging oxygen atoms in the silicate structure [24]. However, for the precipitation of vitusite crystal to occur, Nd polyhedra that form during the heat treatment process require Na⁺ ions as charge compensators. Therefore, Na⁺ ions diffuse into the crystalline phases. The appearance of the second shell (Fig. 5) after crystallization supports the preferential distribution of Na⁺ near Nd³⁺. In addition, this enrichment of Na⁺ (21.4 at%) and P⁵⁺ (14.3 at%) ions inside the crystalline phase results in the reduction of their concentrations in the amorphous phase [8], which can enhance the chemical durability of GCs because Na⁺ is known to initiate reactions with water. It is well known Na⁺ ions start to exchange with H⁺ (or H₃O⁺) ions at the glass surface at the initial stage of corrosion of alkali-silicate glass [25]. In our GCs, the concentration of Na⁺ on the surface (or near the surface) decreased due to the formation of the vitusite crystal containing a large number of Na⁺ ions. Therefore, one can expect higher durability from GCs as compared to pristine glass. A decrease in the normalized released values for Na⁺ (23.67 g/m²) and P⁵⁺ (1.754 g/m²) in the vitusite GCs from the product consistency test as compared to those of the pristine glass (Na: 25.79 g/m², P: 20.62 g/m²) supports this proposition [8].

4. Conclusions

Local environments of Nd ions in vitusite GC waste forms were analyzed using EXAFS spectroscopy. The results of the best fit of the EXAFS spectra suggest that the first shell corresponds to the Nd–O pair with an interatomic distance of 0.24 nm and CNs of 6.7–6.9. The second shell in the GC spectrum is attributed to the combination of Nd–Na and Nd–P pairs. P⁵⁺, Nd³⁺, and Na⁺ ions preferentially accumulated inside the vitusite crystal of the GC waste forms. Because the crystals are encapsulated in the glass matrix, the leaching rates of these ions decreased with the formation of the crystals. These results can be used in the development of new rare-earth waste forms with high chemical durability.

Acknowledgements

This work was supported by the National Research Foundation of Korea (NRF) grant funded by the Korean government (MSIP: Ministry of Science, ICT and Future Planning) (No. NRF-2015M2A7A1000191 & NRF-2015M2A8A5021709). NCH is grateful to the NDA and Royal Academy of Engineering for financial support and EPSRC under grants EP/M026566/1, EP/L018616/1 and EP/L014041/1.

References

[1] T. Inque, L. Koch, Development of pyroprocessing and its future direction, Nucl.

- Eng. Technol. 40 (2008) 183.
- [2] H.S. Lee, J.M. Hur, J.G. Kim, D.H. Ahn, Y.Z. Cho, S.Y. Paek, Korean pyrochemical process R & D activities, Energy Procedia 7 (2011) 391–395.
- [3] J.J. Laidler, J.E. Battles, W.E. Miller, J.P. Ackerman, E.L. Carls, Development of pyroprocessing technology, Prog. Nucl. Energy 31 (1997) 131–140.
- [4] H.S. Lee, G.I. Park, K.H. Kang, J.M. Hur, J.G. Kim, D.H. Ahn, Y.Z. Cho, E.H. Kim, Pyroprocessing technology development at KAERI, Nucl. Eng. Technol. 43 (2011) 317–328.
- [5] D. Caurant, O. Majerus, P. Loiseau, I. Bardez, N. Baffier, J.L. Dussossoy, Crystallization of neodymium-rich phases in silicate glasses developed for nuclear waste immobilization, J. Nucl. Mater. 354 (2006) 143–162.
- [6] C. Liu, J. Heo, Electron energy loss spectroscopy analysis on the preferential incorporation of Er³⁺ ions into fluoride nanocrystals in oxyfluoride glass-ceramics, J. Am. Ceram. Soc. 95 (7) (2012) 2100–2102.
- [7] W. Lutze, R.C. Ewing, Radioactive Waste Forms For The Future, Elsevier Science Pub. Co., NY (USA), 1988, pp. 203–314.
- [8] M. Kim, J. Heo, Vitusite glass-ceramics waste forms form immobilization of lanthanide wastes generated by pyroprocessing, Ceram. Int. 41 (2015) 6132–6136.
- [9] M.D. O'Donnell, S.J. Watts, R.V. Law, R.G. Hill, Effect of P₂O₅ content in two series of soda lime phosphosilicate glasses on structure and properties—part II: physical properties, J. Non-Cryst. Solids 354 (2008) 3561–3566.
- [10] B.H. Toby, EXPGUI, a graphical user interface for GSAS, J. Appl. Cryst. 34 (2001) 210–213.
- [11] J.H. Lambert, On the Measure and Gradations of Light, Colors, and Shade, Eberhardt Klett, Germany, 1760, pp. 391–395.
- [12] M. Newville, EXAFS analysis using FEFF and FEFFIT, J. Synchrotron Rad. 8 (2001) 96–100.
- [13] P. Zalden, C. Bichara, J. van Eijk, C. Braun, W. Bensch, M. Wuttig, Atomic structure of amorphous and crystallized Ge₁₅Sb₈₅, J. Appl. Phys. 107 (2010) 104312.
- [14] S. Kelly, Basics of EXAFS data analysis. Electronic Resource, 2009.
- [15] Y. Zhang, A. Karatutlu, O. Ersoy, W. Little, G. Cibin, A. Dent, A. Sapelkin, Structure and effects of annealing in colloidal matrix-free Ge quantum dots, J. Synchrotron Rad. 22 (2015) 105–112.
- [16] M. Risch, A. Grimaud, K.J. May, K.A. Stoerzinger, T.J. Chen, A.N. Mansour, Y. Shao-Horn, Structural changes of cobalt-based perovskites upon water oxidation investigated by EXAFS, J. Phys. Chem. C 117 (2013) 8628–8635.
- [17] The International Union of Crystallography, Online dictionary of crystallography, 12 Apr, (http://reference.iucr.org/dictionary/R_factor), 2016.
- [18] I. Bardez, D. Caurant, P. Loiseau, N. Baffier, J.L. Dussossoy, C. Gervais, F. Ribot, D.R. Neuville, Structural characterisation of rare earth rich glasses for nuclear waste immobilization, Phys. Chem. Glass. 46 (2005) 320–329.
- [19] M. Karabulut, G.K. Marasinghe, E. Metwalli, A.K. Wittenauer, R.K. Brow, Phys. Rev. B 65 (2002) 101–107.
- [20] R. Salmon, C. Parent, M. Vlasse, G. Flem, The crystal structure of a new high-Nd-concentration laser material: Na₃Nd(PO₄)₂, Mat. Res. Bull. 13 (1978) 439–444.
- [21] K. Momma, F. Izumi, VESTA: a three-dimensional visualization system for electronic and structural analysis, J. Appl. Cryst. 41 (2008) 653–658.
- [22] E.J. Elzinga, R.J. Reeder, S.H. Withers, R.E. Peale, R.A. Mason, K.M. Beck, W.P. Hess, EXAFS study of rare-earth element coordination in calcite, Geochim. Cosmochim. Acta 66 (2002) 2875–2885.
- [23] R.T. Downs, M. Hall-Wallace, The American Mineralogist crystal structure database, Am. Mineral. 88 (2003) 247–250.
- [24] A.K. Varshneya, Fundamentals of Inorganic Glasses, second edition, Elsevier, NY, 2006, pp. 113–118.
- [25] P. Frugier, S. Gin, Y. Minet, T. Chave, B. Bonin, N. Godon, G. Santarini, SON68 nuclear glass dissolution kinetics: current state of knowledge and basis of the new GRAAL model, J. Nucl. Mater. 380 (2008) 8–21.